Science
AAAS

Dynamics of Dpp Signaling and Proliferation Control
O. Wartlick, *et al.*
Science **331**, 1154 (2011);
DOI: 10.1126/science.1200037

Science (print ISSN 0036-8075; online ISSN 1095-9203) is published weekly, except the last week in December, by the American Association for the Advancement of Science, 1200 New York Avenue NW, Washington, DC 20005.

Dynamics of Dpp Signaling and Proliferation Control

O. Wartlick,[1]* P. Mumcu,[2]* A. Kicheva,[1]*† T. Bittig,[2]* C. Seum,[1] F. Jülicher,[2]‡ M. González-Gaitán[1]‡

Morphogens, such as Decapentaplegic (Dpp) in the fly imaginal discs, form graded concentration profiles that control patterning and growth of developing organs. In the imaginal discs, proliferative growth is homogeneous in space, posing the conundrum of how morphogen concentration gradients could control position-independent growth. To understand the mechanism of proliferation control by the Dpp gradient, we quantified Dpp concentration and signaling levels during wing disc growth. Both Dpp concentration and signaling gradients scale with tissue size during development. On average, cells divide when Dpp signaling levels have increased by 50%. Our observations are consistent with a growth control mechanism based on temporal changes of cellular morphogen signaling levels. For a scaling gradient, this mechanism generates position-independent growth rates.

Growth regulation of the *Drosophila* wing imaginal disc critically depends on the Dpp morphogen gradient (*1*–*7*). Dpp mutant imaginal discs fail to grow, and ectopic expression of Dpp in clones of wing cells organizes growth and elicits the formation of an ectopic winglet (*7*). Growth of imaginal discs is spatially homogeneous. How a graded Dpp signal can control homogeneous tissue growth is an open question for which a number of models have been proposed: For example, it has been suggested that the steepness of the gradient (*5*, *8*) and/or mechanical feedback (*9*, *10*) control proliferation. However, little quantitative data supports these models. To address this, we quantified spatial and temporal changes of Dpp concentration, signaling activity, and disc growth parameters during development.

The Dpp gradient scales with wing size. We used a functional green fluorescent protein–Dpp (GFP-Dpp) fusion (*11*, *12*) expressed in the endogenous Dpp source to quantify GFP-Dpp profiles as a function of distance x from the source at different times t during larval development (Fig. 1, A to C), both with and without expression of the endogenous Dpp gene (*13*) (fig. S1). During the growth period, the Dpp gradient expands: Both the gradient amplitude C_0 (i.e., the concentration at the source boundary) and the decay length λ (the distance λ over which the gradient decays) increase significantly (Fig. 1, D and E). The decay length, λ, is proportional to the target tissue width L [the scaling ratio $\lambda/L = 0.112$ is constant; Fig. 2, A and B; n = two independent data sets with $\lambda/L = 0.107$ ($n_1 = 98$ discs) and $\lambda/L = 0.116$ ($n_2 = 60$ discs); table S3]. Further analysis of Dpp gradient profiles, $C(r,t)$, where $r = x/L$ is the relative distance to the source, revealed that the relative concentration gradient, $C(r,t)/C_0(t)$, is invariant during development (Fig. 2A); the gradient scales with the growing tissue. Gradient scaling behaviors have been reported in this and other systems (*14*–*17*), and possible mechanisms have been discussed (*18*, *19*) [supporting online material (SOM) text S1.2]. Note that the gradient of another morphogen, Hedgehog (Hh), does not scale (fig. S2).

Decreasing degradation accounts for gradient expansion. Gradient expansion is not due to stretching of the gradient by wing growth, because the Dpp degradation rate is much larger than the disc growth rate; the gradient renews itself faster than the tissue grows (SOM text S1.1). Hence, gradient expansion is due to changes in Dpp production (ν), diffusion (D), or degradation (k) (*12*, *20*) (SOM text S1.1). Estimation of these parameters by fluorescence recovery after photobleaching (FRAP) (*12*) and a reporter assay [SOM quantitative procedures (QP) 3] showed that Dpp production and diffusion vary only slightly during the growth phase (Fig. 2, C and D), whereas the degradation rate decreases substantially as $k \sim 1/A$ with increasing posterior compartment area A (Fig. 2E). This decrease of the degradation rate could account for the constant scaling ratio λ/L, because $\lambda = \sqrt{D/k}$ and $A \sim L^2$ (*12*, *21*) (SOM text S1.2). Furthermore, the gradient amplitude, C_0, also increases, because of the decreasing degradation rate and the widening of the Dpp source (w) (Fig. 2F) (SOM text S1.1). Thus, changes of the Dpp source width and trafficking (degradation rate) result in Dpp gradient expansion during growth.

Cells experience an increase in Dpp concentration. Gradient expansion implies that cellular Dpp concentration changes over time. Two factors determine the cellular Dpp concentration: changes of the gradient profile (Fig. 1) and changes in cell position, $x_{cell}(t)$, in the growing tissue. Proliferation is approximately homogeneous in space (*22*, *23*) (figs. S3A and S4A), so the relative position of a cell, $r_{cell} = x_{cell}(t)/L(t)$, remains constant as the tissue grows (fig. S3A; SOM QP5). Because r_{cell} is constant and the relative concentration gradient $C(r,t)/C_0(t)$ is invariant (Fig. 2A), the relative cellular concentration, $C(r_{cell},t)/C_0(t)$, is constant during development. Therefore, the average cellular Dpp concentration, $C_{cell}(t) = C(r_{cell},t)$, increases proportionally to the gradient amplitude, $C_0(t)$ (fig. S4C).

The Dpp concentration increases, on average, by 40% during each cell cycle. Does the increase in cellular Dpp concentration correlate with changes in the proliferation rate? We determined the proliferation rate (fig. S5; SOM QP4) from the area growth rate, $g = \dot{A}/A$, where $\dot{A}$ is the time derivative of the area A. This is a good approximation for the cellular proliferation rate because the cell density only shows a minor increase during wing growth (fig. S5, B and D). During the growth phase, the growth rate (g) decreases (fig. S5D), which reflects an increasing cell doubling time θ ($\theta \approx \ln 2/g$; SOM QP1), mostly because of a lengthening of the G_2 phase (*24*) (fig. S6).

We found that area growth correlates with the increase of the gradient amplitude by a power law (Fig. 2G)

$$C_0(t) \sim A(t)^{\beta} \qquad (1)$$

where $\beta = 0.59$ (n = two data sets; table S3). The average cellular Dpp concentration, C_{cell}, is proportional to the amplitude C_0 (see above) and therefore, $C_{cell}(t) \sim A(t)^{\beta}$. Derivation of this expression with respect to time reveals a correlation of the average growth rate ($g = \dot{A}/A$) with average temporal changes in the Dpp level ($\dot{C}_{cell}$) perceived by cells: $\dot{C}_{cell}/C_{cell} = \dot{C}_0/C_0 = \beta(\dot{A}/A) = \beta g$. Because the area growth rate and the cellular proliferation rate g_{cell} are approximately equal (see above), it follows that

$$g_{cell} \approx \frac{1}{\beta}\frac{\dot{C}_{cell}}{C_{cell}} \qquad (2)$$

i.e., the proliferation rate is proportional to relative temporal changes of Dpp.

To estimate the relative increase of the cellular Dpp concentration $\alpha = \Delta C_{cell}/C_{cell}$ during the cell cycle time θ, we combine Eq. 2 with the approximations $\dot{C}_{cell}/C_{cell} \approx (\Delta C_{cell}/\theta)/C_{cell}$ and $\theta \approx \ln 2/g_{cell}$, and obtain the following:

$$\alpha = \frac{\Delta C_{cell}}{C_{cell}} \approx \beta \ln 2 \qquad (3)$$

Thus, we find a constant $\alpha = 0.41$ (n = two data sets; table S3); throughout development, cell division correlates with an increase of Dpp concentration by 40%.

[1]Departments of Biochemistry and Molecular Biology, Faculty of Sciences, Geneva University, 30 Quai Ernest-Ansermet, 1211 Geneva, Switzerland. [2]Max Planck Institute for the Physics of Complex Systems, Nöthnitzer Strasse 38, 01187 Dresden, Germany.

*These authors contributed equally to this work.

†Present address: Developmental Neurobiology, National Institute for Medical Research, Medical Research Council, The Ridgeway, Mill Hill, London NW71AA, UK.

‡To whom correspondence should be addressed. E-mail: julicher@pks.mpg.de (F.J.), marcos.gonzalez@unige.ch (M.G.-G.)

Dpp signaling activity parallels Dpp concentration. Proliferation depends on Dpp signaling activity, rather than ligand concentration (*3*, *25*–*27*). We therefore measured Dpp pathway activity at different levels [reviewed in (*28*)]: phosphorylated Mad (P-Mad) (*29*), P-Mad/Medea complex formation, and *brk* and *dad* transcription [Fig. 3A and fig. S7; SOM experimental procedures (EP) 1] (*30*, *31*). Of these, we systematically analyzed nuclear red fluorescent protein expressed under control of the dad enhancer (dad-nRFP) as a transcriptional readout reflecting cellular signaling activity, S_{cell}.

With time-lapse analysis, we confirmed that Dpp signaling increases in living wing discs (Fig. 3B and movie S1). Consistent with Eq. 2, relative changes in signaling, $\dot{S}/S$, are larger at early times of development, when growth is faster. Quantification of dad-nRFP profiles, $S(r,t)$ (Fig. 3C), in fixed discs showed that (i) the signaling gradient scales (Fig. 3D), i.e., the scaling ratio λ_s/L is constant (Fig. 3E); and (ii) the amplitude S_0 increases with A as a power law (Eq. 1), with $\beta_s = 0.69 \pm 0.02$ (SEM) (n = four data sets; table S3), corresponding to $\alpha_s = 48\% \pm 2\%$ (Fig. 3F). Invariance (scaling) of the relative signaling profile, $S(r,t)/S_0(t)$ (Fig. 3D), implies that the cellular signaling level is proportional to the amplitude ($S_{cell} \sim S_0$). The power-law relation between amplitude S_0 and area A (Fig. 3F) indicates that the proliferation rate correlates with the average relative temporal increase of Dpp signal, $\dot{S}_{cell}/S_{cell} = \dot{S}_0/S_0$ (as in Eq. 2):

$$g_{cell} \approx \frac{\ln 2}{\alpha_s}\frac{\dot{S}_{cell}}{S_{cell}} \qquad (4)$$

Here, $\alpha_s = 48\%$ implies that the cellular Dpp signaling level S_{cell} increases by about 50% during each cell cycle. On the basis of Eq. 4, we propose a model of growth control where the cell cycle length is determined by how fast an increase of cellular Dpp signal by 50% is achieved.

In different growth regimes, $\alpha_s \approx 50\%$. Dpp source and transport parameters contribute to the amplitude S_0 (SOM text S1.1) and therefore to cellular signaling levels S_{cell}. To test how the rate of increase of the gradient amplitude affects growth, we analyzed three conditions with changed Dpp source and/or transport parameters (SOM EP2): (i) haltere discs, where we found that Dpp production, diffusion, and degradation are smaller (*32*, *33*) (Fig. 2, C to F; SOM QP3.2); (ii) wing discs with a Dpp source of haltere histotype (dpp>Ubx) (*32*, *33*); and (iii) wing discs with a constant one-cell-wide source [limiting Hh signaling range to one cell with membrane-tethered Hh (Hh-CD2)] (*34*).

In these tissues, the decay time of the growth rate, the growth period, and final size differ from that of the wild-type wing disc (table S2 and fig. S8). However, growth and Dpp signaling still are related by the same features: (i) Gradients scale with tissue size. The scaling ratio λ/L is constant,

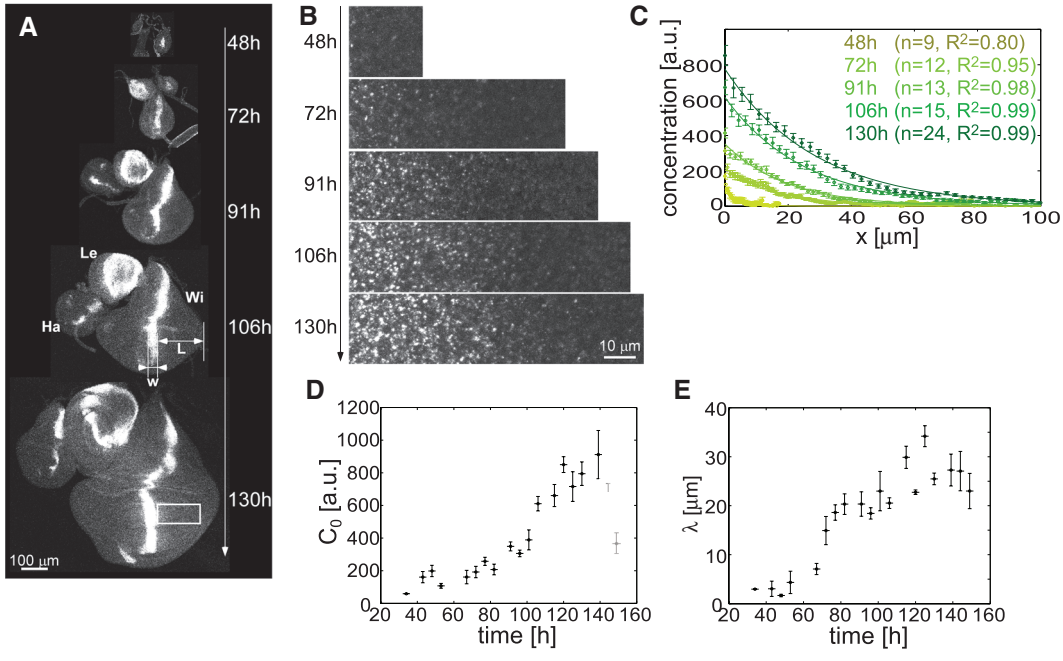

Fig. 1. Dpp gradient parameters. (**A**) *dpp-Gal4/UAS-GFP-Dpp* wing (Wi), leg (Le), and haltere (Ha) discs at different developmental times; w, source width, L, target width. (**B**) Images of GFP-Dpp gradients, corresponding to boxed areas in (A). (**C**) Quantification of GFP-Dpp concentration as a function of the distance to the source (x). (**D** and **E**) (D) Amplitude, C_0 and (E) decay length, λ, over time. At the end of the growth phase, in prepupal discs ($t > 140$ hours), C_0 again decreases. Error bars correspond to standard errors (SEM) of averages from binned data, and one data set per graph is shown. For fit functions, parameters, number of data sets, and number of discs per data set, see tables S1 to S3 and SOM QP1. For extended versions of figure legends, see SOM.

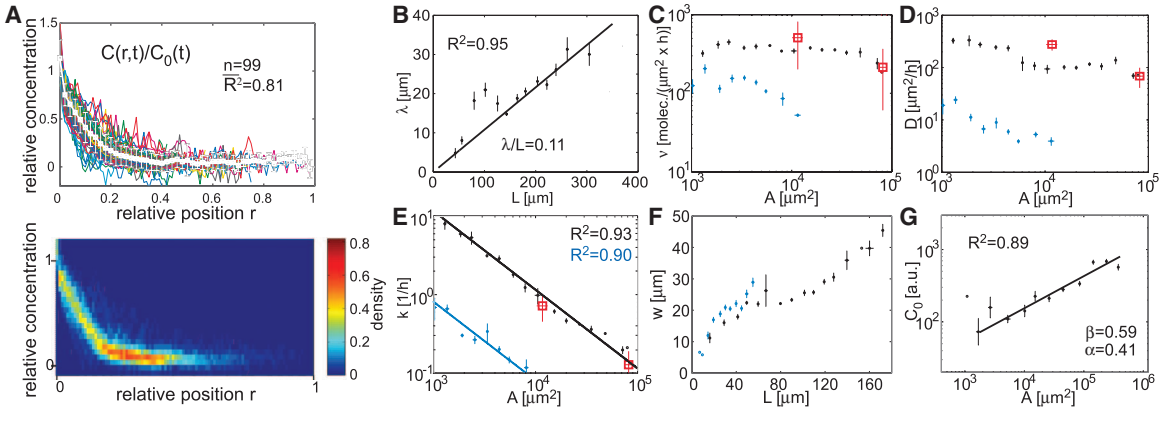

Fig. 2. The Dpp gradient and growth. (**A**) Relative Dpp concentration profiles $C(r,t)/C_0$ from 48 hours to 130 hours (spanning the whole growth period) with density plot (below). Note the data collapse of gradient profiles onto a single curve. (**B**) Decay length, λ, versus compartment width, L. (**C** to **F**) (C) Dpp production rate, ν; (D) diffusion coefficient, D; and (E) degradation rate, k, versus posterior compartment area, A; and (F) Dpp source width, w, versus posterior compartment width, L, of wing (black) and haltere (blue) discs during growth, estimated by FRAP (red rectangles, wing) and a reporter assay (circles) (SOM QP3). (**G**) Gradient amplitude, C_0, versus posterior compartment area, A.

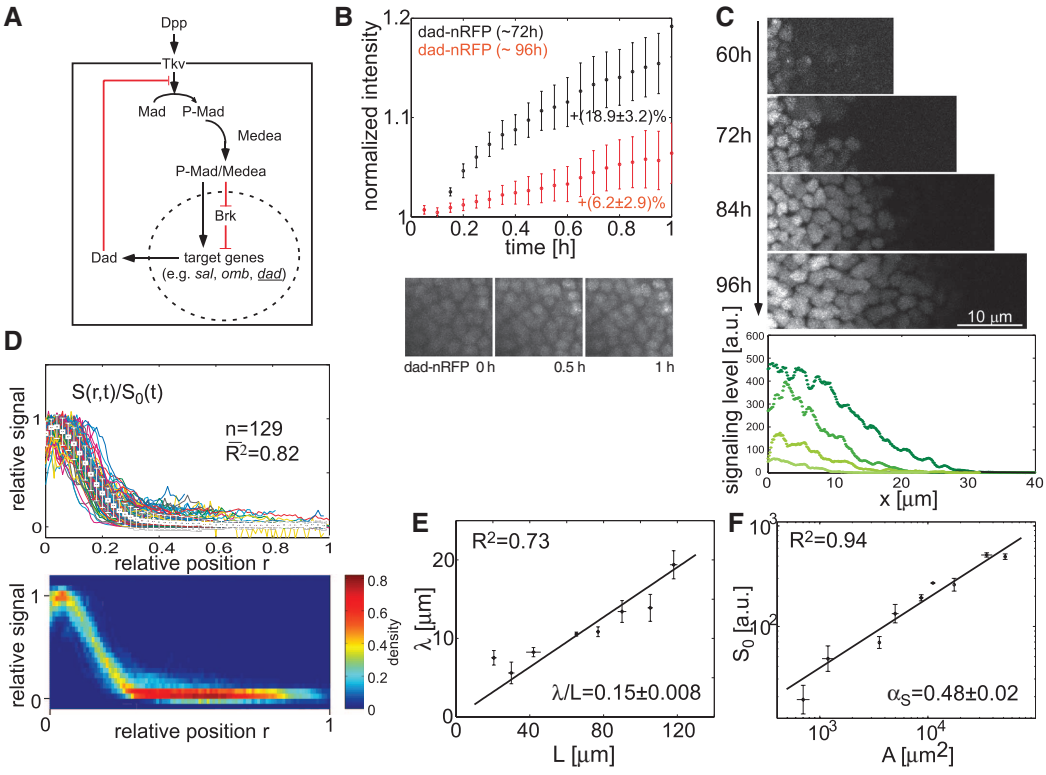

Fig. 3. Dpp signaling gradients. (**A**) Dpp pathway. (**B**) Average dad-nRFP intensity over time for time-lapse series at 72 and 96 hours of development (SOM QP6). Below, frames from a time-lapse series. (**C**) dad-nRFP images with quantification (60-hour and 72-hour images are contrasted). (**D**) Relative signaling profiles, $S(r, t)/S_0(t)$, spanning the whole growth period, with density plot. Profiles collapse onto a single curve. (**E** and **F**) (E) Decay length, λ, versus L and (F) amplitude, S_0, versus A.

but different, in the different conditions (Fig. 4A and fig. S9), the relation between decay length and area is the same in all conditions except Hh-CD2 (Fig. 4C; SOM text S1.2). This points to a possible role of Hh for scaling. (ii) g and $\dot{S}_{cell}/S_{cell}$ are proportional during growth (Fig. 4B). And (iii), α_s is similar under all these conditions (Fig. 4D; mean of $\alpha_s = 49\% \pm 2\%$). Thus, cells divide when Dpp signaling levels have increased by about 50%, regardless of histotype (haltere versus wing), Dpp transport dynamics, or Hh signaling in the source.

A scaling mutant shows inhomogeneous growth while $\alpha_s \approx 50\%$. In all conditions discussed, the gradient scales, and proliferation is spatially uniform. In contrast, proliferation is not homogeneous when Dpp is ubiquitously expressed with the C765-Gal4 driver (C765>Dpp): Lateral positions have a larger growth rate (*27*). We quantified Dpp signaling and growth parameters in C765>Dpp to determine whether $\dot{S}_{cell}/S_{cell}$ is related to the local inhomogeneous growth rates in a manner consistent with Eq. 4.

In C765>Dpp discs, the spatial signaling profiles $S(r,t)$ increase over time, but do not scale (Fig. 5, A and B). We quantified the inhomogeneities of the growth rate, $g(r,t)$, using spatial profiles of phosphorylated histone H3 (PH3)–positive mitotic cells (Fig. 5C and fig. S3B; SOM QP4 and QP5). From $g(r,t)$ and $S(r,t)$, we then estimated g_{cell}, $\dot{S}_{cell}/S_{cell}$, and α_s for cells at different positions, $r_{cell}(t)$ (Fig. 5; SOM QP6). We noted that cells divide as they do in wild type when Dpp signaling levels have increased by about 50%, independent of time and cell position (Fig. 5D). Lack of scaling causes position

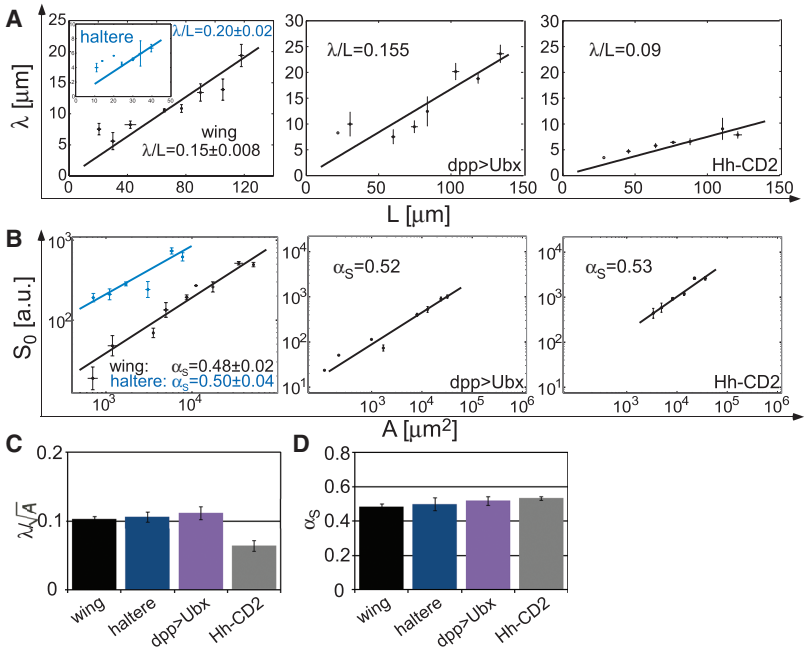

Fig. 4. Dpp signaling and growth in different growth conditions. (**A** and **B**) (A) dad-nRFP decay length, λ, versus L and (B) amplitude, S_0, versus A for wing and haltere discs (n = four data sets; table S3); "haltere-wing chimera" (dpp>Ubx; $n = 2$); and the "one-cell-wide source" experiments (Hh-CD2; $n = 2$). (**C** and **D**) (C) Scaling ratio $\lambda/\sqrt{A}$ and (D) coefficient α_S.

dependence of $\dot{S}_{cell}/S_{cell}$ (SOM text S1.3), and thus, higher lateral growth rates are explained by the fact that the relative increase α_s is reached faster (i.e., $\dot{S}_{cell}/S_{cell}$ is larger) in lateral positions.

Exogenous manipulation of $\dot{S}_{cell}/S_{cell}$ results in predictable growth rates. To further test whether cells divide when Dpp signaling levels increase by 50%, we used an established method to conditionally express the constitutively active Dpp receptor, Tkv^{QD}, in cell clones (*5*) (Fig. 6). Here, Tkv^{QD} transcription is induced exogenously, only after adding the progesterone-analog drug mifepristone (RU486) (*5*) (SOM EP2). In our model, exogenous manipulation of $\dot{S}_{cell}/S_{cell}$

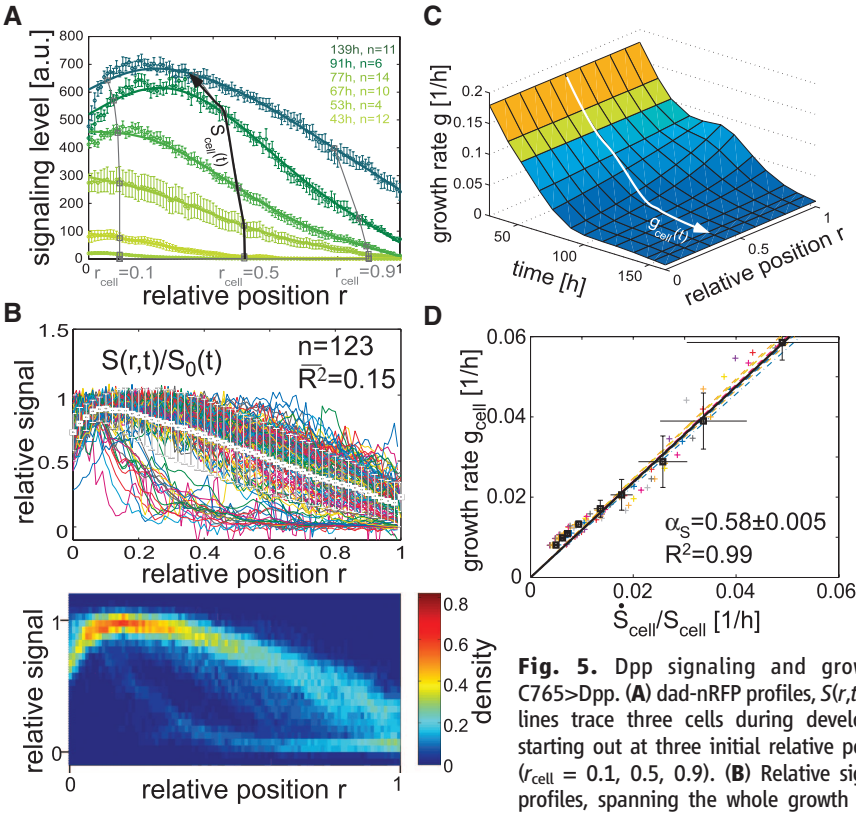

Fig. 5. Dpp signaling and growth in C765>Dpp. (**A**) dad-nRFP profiles, $S(r,t)$; black lines trace three cells during development starting out at three initial relative positions (r_{cell} = 0.1, 0.5, 0.9). (**B**) Relative signaling profiles, spanning the whole growth period, with density plot. Profiles do not collapse onto a single curve. (**C**) Spatiotemporal growth profile, $g(r,t)$; white arrow traces cell starting out at r_{cell} = 0.5. (**D**) Growth (g) versus $\dot{S}_{cell}/S_{cell}$ of cells starting out at different relative positions (r_{cell} = 0.1, …, 0.9; different colors).

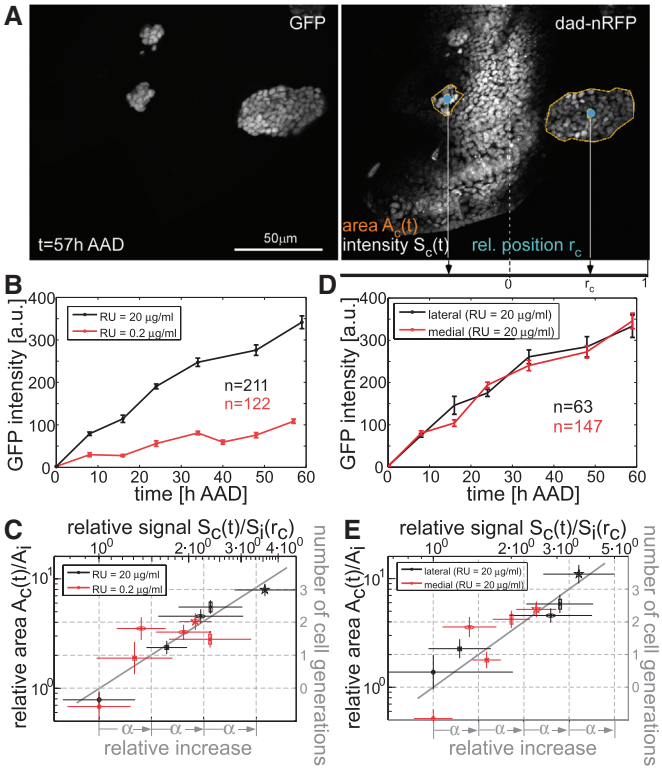

Fig. 6. Tkv^{QD} clones (SOM EP2/QP7). (**A**) (Left) Tkv^{QD} clones marked by GFP; (right) dad-nRFP; relative position r_c, area A_c and average signaling level S_c of clones were measured in discs at different times after Tkv^{QD} induction [hours after addition of drug (h AAD)]. Genotype: *y w hsFlp/UAS-p35; dad-nRFP/UAS-GFP; act>y>Gal4: PR/UAS-Tkv^{QD}*. (**B** and **D**) Average GFP intensity, reflecting Tkv^{QD} and p35 expression level for (B) different drug concentrations and (D) medial versus lateral clones. (**C** and **E**) Relative increase in clone area with respect to the initial area, A_c/A_i, versus relative increase in Dpp signaling levels, S_c/S_i (r_c). For determination of A_i and S_i, see SOM QP7. Symbols in (C) and (E) indicate data points at different times AAD. Gray line (our model): For every signaling increase by α_S = 50%, clone area is expected to double, i.e., the cell generation number increases by 1.

in clones should result in clonal growth rates quantitatively predicted by Eq. 4.

For an RU486 concentration of 20 µg/ml, Gal4 activity (and, therefore, Tkv^{QD} expression) increases 3.6 times as fast as at 0.2 µg/ml; i.e., in these two experiments, $\dot{S}_{cell}$ is different (Fig. 6B). The relative increase in signaling levels in clones, $\dot{S}_{cell}/S_{cell}$, therefore, depends on RU486 concentration, as well as on the initial endogenous signaling level: Although exogenously imposed $\dot{S}_{cell}$ is the same in medial and lateral regions of the disc (Fig. 6D), clones in lateral positions experience a bigger relative increase in signaling upon Tkv^{QD} induction because their initial signaling level is lower, i.e., $\dot{S}_{cell}/S_{cell}$ is dependent on clone position (fig. S10). If growth is causally controlled by $\dot{S}_{cell}/S_{cell}$, then RU486 concentration, clone position, and duration of drug exposure should determine the clone area, whereas α_s should be independent of these parameters.

The growth rate of clones indeed correlates with the exogenously imposed $\dot{S}_{cell}/S_{cell}$; i.e., the relative increases in clone area and in signaling level are correlated by a power law (Fig. 6, C and E; SOM QP7). The data are remarkably consistent with $\alpha_s \approx 50\%$, independently of RU486 concentration, duration of exposure (Fig. 6, B and C), and clone position (Fig. 6, D and E). Thus, local exogenous changes of $\dot{S}_{cell}/S_{cell}$ locally result in proliferation rates predicted by Eq. 4.

Simulation of growth control. To further test whether Eq. 4 describes a plausible growth mechanism, we developed a two-dimensional physical description of proliferation control [Fig. 7 and movies S2 to S5; SOM simulation (SI)]. We implemented Dpp and Hh production, diffusion, and degradation in a discrete vertex model that describes cells as polygons and accounts for the mechanical properties of the tissue (*35*). Dpp source cells are selected in response to Hh; Dpp production and diffusion are kept constant; and the Dpp degradation rate is dynamically altered in response to cell division events, such that the average degradation rate in the tissue becomes inversely proportional to the cell number (consistent with Fig. 2, C to F). A cell divides when the relative increase of the local Dpp level reaches a threshold α.

Simulations of this model using parameter values estimated experimentally for wing and haltere discs result in growth dynamics that quantitatively match the experimental observations for wing and haltere discs (Fig. 7, D to F, and movie S3), although only the initial cell number, minimal cell cycle length, and Dpp diffusion and degradation are different in the haltere. Furthermore, simulations of our model can account for the growth properties of Tkv^{QD} clones: Consistent with previous experimental results (*3*, *5*), simulated lateral Tkv^{QD} clones have a bigger growth rate and grow to a larger size than medial Tkv^{QD} clones (about 4-fold and 2.5-fold as large as simulated wild-type clones, respectively) (Fig. 7, G to I), and cells surrounding Tkv^{QD} clones overproliferate (Fig. 7G; SOM text S2). These

results indicate that growth control by means of relative changes in Dpp levels could underlie growth control during imaginal disc development.

Conclusion. We have shown here that, in the wild type, Dpp concentration and signaling gradients scale and that, on average, cells divide when Dpp signaling levels have increased by $\alpha_s \approx 50\%$. A growth mechanism based on relative changes in signaling levels can quantitatively account for growth dynamics of wing and haltere discs, for inhomogeneous growth observed in scaling mutants, and for growth properties of Tkv^{QD} clones. Other growth-control mechanisms we considered—for example, mechanisms based on spatial differences in Dpp concentration or signaling—are less consistent with our data (SOM text S1.3.2). However, the growth rule proposed here remains to be verified on the single-cell level.

Would the growth mechanism proposed here work in the entire wing? In wild-type discs, our Dpp concentration and signaling measurements were only significantly above background in medial regions. However, the C765>Dpp and Tkv^{QD} clone experiments show that the $\dot{S}_{cell}/S_{cell}$ mechanism also works laterally. Furthermore, in our simulations of wild-type disc growth, Dpp molecule numbers in lateral regions are low but sufficient to provide enough precision to control proliferation by a temporal growth rule (SOM SI8). The simulations indeed capture the main growth properties of the complete wing and haltere, which indicates that the growth mechanism could in principle operate globally.

How could cells determine relative increases in Dpp signaling? Sensitivity of signaling systems to relative changes of input is typical for adaptive sensory systems and plays a role in bacterial and sperm chemotaxis and in olfactory and visual transduction, where determination of relative temporal changes is achieved by combining adaptation with a dynamic response (*36*–*40*). The

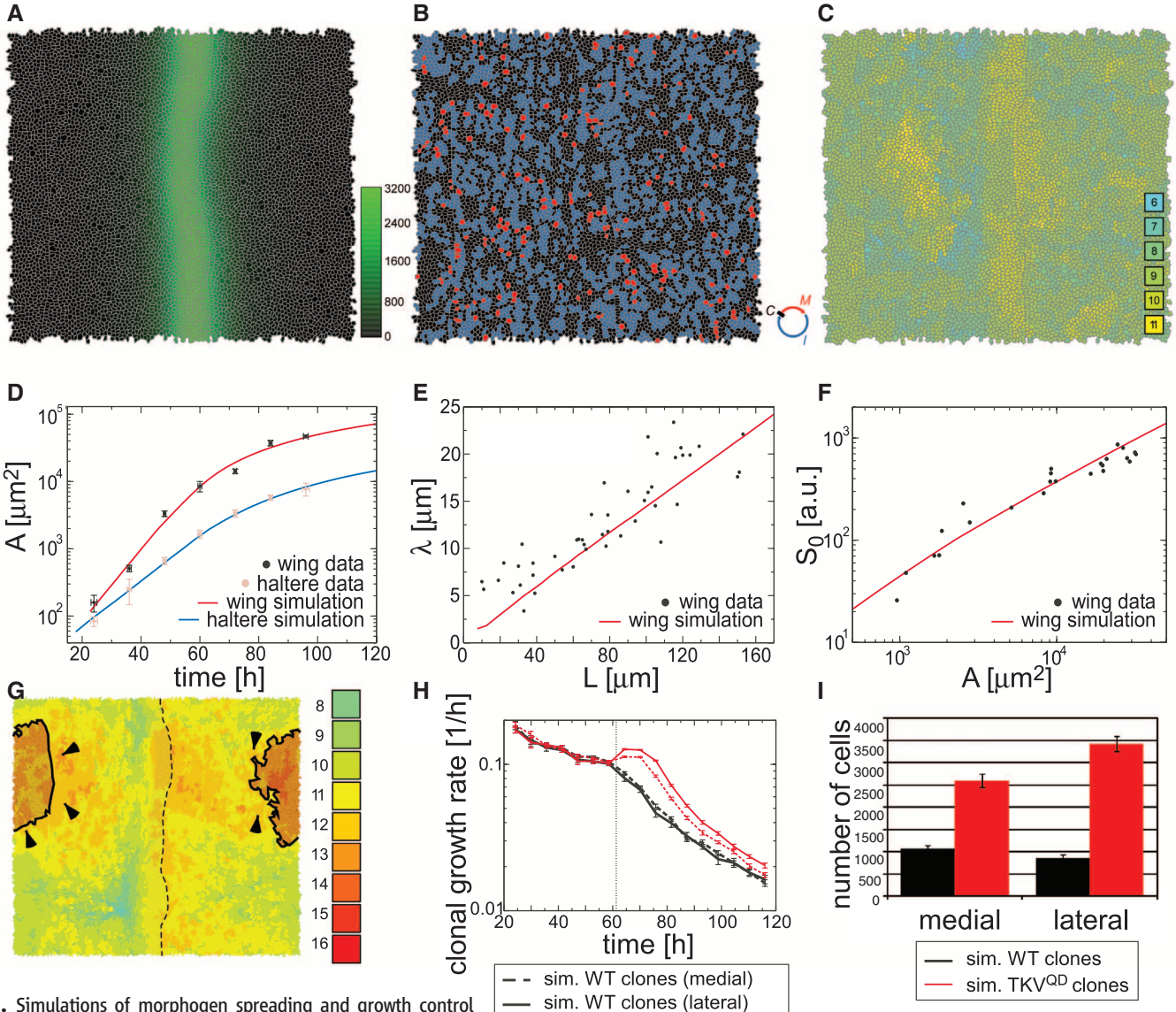

Fig. 7. Simulations of morphogen spreading and growth control (SOM SI). (**A** to **C**) Representative sample of simulation results. (A) Simulated Dpp distribution; color intensity code: number of Dpp molecules. (B) Cell cycle state [red, *M* (M phase); blue, *I* (constant phase in interphase); black, *C* (checkpoint phase)]. (C) Cell generation number (color-coded). (**D** to **F**) Averaged simulation results (red and blue, $n = 25$) with experimental data (black and gray). (D) Posterior compartment area over time. (E) Decay length versus posterior compartment width. (F) Gradient amplitude versus posterior compartment area. (**G** to **I**) Numerical simulations of wild-type and Tkv^{QD} clones located close to and far from the source ("medial" and "lateral," respectively). (G) Lateral clone expressing Tkv^{QD} (black outline; dashed line, AP boundary) with cell generation number (color-coded); note nonautonomous effects on proliferation around the clone (arrowheads). (H) Average growth rates of simulated medial and lateral Tkv^{QD} (red) and control (black) clones ($n=25$); vertical dashed line: induction of Tkv^{QD} production; I, average simulated clone size at $t = 120$ hours.

Dpp pathway is a dynamic network and may generate adaptive responses by combining feed-forward and feedback elements in its structure. Consistent with this idea, in brk^{XA} mutants, where the Dpp network is perturbed, α_s has a different value (fig. S11) [This mutant is discussed in detail in SOM text S2.4].

Our observations raise the question of what molecular mechanisms underlie (i) cell cycle control via relative temporal changes of Dpp signaling, (ii) gradient scaling via decrease of Dpp degradation, and (iii) final size determination. Although pupariation time and final size were different in the different conditions studied, the average cell cycle length at pupariation was about 30 hours for all (table S2; SOM text S1.3.4), which suggested that cells could stop dividing when their cell cycle is prolonged beyond a threshold. Response to this threshold could be deregulated in some tumor mutants.

References and Notes

1. J. Capdevila, I. Guerrero, *EMBO J.* **13**, 4459 (1994).
2. T. Lecuit *et al*., *Nature* **381**, 387 (1996).
3. C. Martín-Castellanos, B. A. Edgar, *Development* **129**, 1003 (2002).
4. D. Nellen, R. Burke, G. Struhl, K. Basler, *Cell* **85**, 357 (1996).
5. D. Rogulja, K. D. Irvine, *Cell* **123**, 449 (2005).
6. F. A. Spencer, F. M. Hoffmann, W. M. Gelbart, *Cell* **28**, 451 (1982).
7. M. Zecca, K. Basler, G. Struhl, *Development* **121**, 2265 (1995).
8. S. J. Day, P. A. Lawrence, *Development* **127**, 2977 (2000).
9. T. Aegerter-Wilmsen, C. M. Aegerter, E. Hafen, K. Basler, *Mech. Dev.* **124**, 318 (2007).
10. L. Hufnagel, A. A. Teleman, H. Rouault, S. M. Cohen, B. I. Shraiman, *Proc. Natl. Acad. Sci. U.S.A.* **104**, 3835 (2007).
11. E. V. Entchev, A. Schwabedissen, M. González-Gaitán, *Cell* **103**, 981 (2000).
12. A. Kicheva *et al*., *Science* **315**, 521 (2007).
13. Materials and methods [experimental procedures (EPs), quantitative procedures (QPs), and simulations (SIs)] along with supporting text (including extended figures legends for text figures), tables, figures, and movies are available as supporting material on *Science* Online.
14. D. Ben-Zvi, B. Z. Shilo, A. Fainsod, N. Barkai, *Nature* **453**, 1205 (2008).
15. T. Gregor, W. Bialek, R. R. de Ruyter van Steveninck, D. W. Tank, E. F. Wieschaus, *Proc. Natl. Acad. Sci. U.S.A.* **102**, 18403 (2005).
16. H. Spemann, H. Mangold, *Roux Arch. Entw. Mech.* **100**, 599 (1924).
17. A. A. Teleman, S. M. Cohen, *Cell* **103**, 971 (2000).
18. N. Barkai, D. Ben-Zvi, *FEBS J.* **276**, 1196 (2009).
19. D. Ben-Zvi, N. Barkai, *Proc. Natl. Acad. Sci. U.S.A.* **107**, 6924 (2010).
20. O. Wartlick, A. Kicheva, M. Gonzalez-Gaitan, *Cold Spring Harbor Perspect. Biol.* **1**, a001255 (2009).
21. H. G. Othmer, E. Pate, *Proc. Natl. Acad. Sci. U.S.A.* **77**, 4180 (1980).
22. A. Garcia-Bellido, J. R. Merriam, *Dev. Biol.* **24**, 61 (1971).
23. M. González-Gaitán, M. P. Capdevila, A. García-Bellido, *Mech. Dev.* **46**, 183 (1994).
24. M. J. Fain, B. Stevens, *Dev. Biol.* **92**, 247 (1982).
25. R. Burke, K. Basler, *Development* **122**, 2261 (1996).
26. E. Moreno, K. Basler, G. Morata, *Nature* **416**, 755 (2002).
27. G. Schwank, S. Restrepo, K. Basler, *Development* **135**, 4003 (2008).
28. M. Affolter, K. Basler, *Nat. Rev. Genet.* **8**, 663 (2007).
29. H. Tanimoto, S. Itoh, P. ten Dijke, T. Tabata, *Mol. Cell* **5**, 59 (2000).
30. A. Weiss *et al*., *Nat. Struct. Mol. Biol.* **17**, 69 (2010).
31. L. C. Yao *et al*., *Development* **135**, 2183 (2008).
32. M. A. Crickmore, R. S. Mann, *Science* **313**, 63 (2006).
33. L. F. de Navas, D. L. Garaulet, E. Sánchez-Herrero, *Development* **133**, 4495 (2006).
34. M. Strigini, S. M. Cohen, *Development* **124**, 4697 (1997).
35. R. Farhadifar, J. C. Röper, B. Aigouy, S. Eaton, F. Jülicher, *Curr. Biol.* **17**, 2095 (2007).
36. U. Alon, M. G. Surette, N. Barkai, S. Leibler, *Nature* **397**, 168 (1999).
37. C. I. Bargmann, *WormBook* (25 October), 1 (2006).
38. N. Barkai, S. Leibler, *Nature* **387**, 913 (1997).
39. B. M. Friedrich, F. Jülicher, *Proc. Natl. Acad. Sci. U.S.A.* **104**, 13256 (2007).
40. L. Zheng *et al*., *PLoS ONE* **4**, e4307 (2009).

41. We thank E. Sánchez-Herrero, S. Cohen, G. Campbell, and K. Irvine for reagents, and M. Milinkovitch, A. Martínez-Arias, T. Ferraro, and F. Naef for discussions. A.K. developed and performed the FRAP and P-Mad assays. O.W. generated all other experimental data and had a leading role to develop the quantitative methods to analyze it. P.M. had a leading role to develop the theoretical description of growth control, and he performed computer simulations. P.M. and T.B. developed a continuum theory of the Dpp gradient during growth and studied possible growth rules. C.S. generated reagents. O.W., P.M., A.K., T.B., F.J., and M.G.-G. developed the whole project synergistically and equally and wrote the paper together. P.M., T.B., and F.J. were supported by the Max-Planck-Gesellschaft. O.W., A.K., C.S., and M.G.-G. were supported by Geneva University and by European Research Council advanced investigator grant (SARA), SystemsX (LipidX), Swiss National Science Foundation (SNF), National Centre of Competence in Research (NCCR) chemical biology and Frontiers in Genetics and R'equip grants.

Supporting Online Material

www.sciencemag.org/cgi/content/full/331/6021/1154/DC1
Materials and Methods
SOM Text
Figs. S1 to S53
Tables S1 to S5
References
Movies S1 to S5

5 November 2010; accepted 6 January 2011
10.1126/science.1200037

Crystal Structure of the Dynein Motor Domain

Andrew P. Carter,[1,2]*† Carol Cho,[1]* Lan Jin,[1] Ronald D. Vale[1]†

Dyneins are microtubule-based motor proteins that power ciliary beating, transport intracellular cargos, and help to construct the mitotic spindle. Evolved from ring-shaped hexameric AAA-family adenosine triphosphatases (ATPases), dynein's large size and complexity have posed challenges for understanding its structure and mechanism. Here, we present a 6 angstrom crystal structure of a functional dimer of two ~300-kilodalton motor domains of yeast cytoplasmic dynein. The structure reveals an unusual asymmetric arrangement of ATPase domains in the ring-shaped motor domain, the manner in which the mechanical element interacts with the ATPase ring, and an unexpected interaction between two coiled coils that create a base for the microtubule binding domain. The arrangement of these elements provides clues as to how adenosine triphosphate–driven conformational changes might be transmitted across the motor domain.

The cytoskeletal motor proteins consist of the myosin family, which moves along actin filaments, and the kinesin and dynein families, which move along microtubules. These motors use a common principle to generate movement in which they bind to their track, undergo a force-producing conformational change, release from the track, and then return to their original conformation. These structural changes are coupled to chemical transitions in the motor's adenosine triphosphatase (ATPase) cycle [adenosine triphosphate (ATP) binding, hydrolysis, and product release].

The force-generating cycles of kinesins and myosins are understood in considerable mechanistic detail. Even though they interact with different cytoskeletal polymers, kinesins and myosins share a protein fold, reflecting their common evolutionary origin (*1*). Dyneins, by contrast, are unrelated to kinesins/myosins and instead have evolved from the AAA family of ATPases (*2*). The AAA ATPases (ATPases associated with diverse cellular activities), which are present in both prokaryotes and eukaryotes, participate in diverse functions, including protein unfolding for proteolysis, disassembly of stable protein complexes, and helicase activities (*3*). The majority of AAA ATPases self-assemble into hexameric rings that carry out the functional activities of these enzymes (*4*, *5*). Dynein is one of two AAA ATPases that has six distinct AAA domains concatenated within a single polypeptide chain [the other being Rea1, an ATPase involved in ribosome biogenesis (*6*)]. Electron microscopy (EM) studies of dynein have shown that these AAA domains fold into a ring-shaped structure similar to other AAA ATPases (*7*–*9*).

[1]Department of Cellular and Molecular Pharmacology, Howard Hughes Medical Institute, University of California–San Francisco, 600 16th Street, San Francisco, CA 94158, USA. [2]Medical Research Council Laboratory of Molecular Biology, Hills Road, Cambridge, CB2 0QH, UK.

*These authors contributed equally to this work.
†To whom correspondence should be addressed. E-mail: cartera@mrc-lmb.cam.ac.uk (A.P.C.); vale@cmp.ucsf.edu (R.D.V.)